Journal Pre-proof

Impact of the pulling rate on the redox state and magnetic domains of Fe-Si-O glass ceramic processed by LFZ method

S.A. Salehizadeh (Investigation) (Formal analysis) (Writing - original draft) (Visualization) (Writing - review and editing), N.M. Ferreira (Investigation) (Writing - review and editing) (Validation), M.S. Ivanov (Investigation) (Writing - review and editing), V.A. Khomchenko (Writing - review and editing) (Resources), J.A. Paixão (Resources), F.M. Costa (Conceptualization) (Writing - review and editing) (Resources), M.A. Valente (Supervision) (Writing - review and editing) (Resources), M.P.F. Graça (Supervision) (Writing - review and editing) (Resources)

PII: S0025-5408(20)31453-7

DOI: https://doi.org/10.1016/j.materresbull.2020.110972

Reference: MRB 110972

To appear in: *Materials Research Bulletin*

Received Date: 25 November 2019

Revised Date: 9 June 2020

Accepted Date: 16 June 2020

Please cite this article as: Salehizadeh SA, Ferreira NM, Ivanov MS, Khomchenko VA, Paixão JA, Costa FM, Valente MA, Graça MPF, Impact of the pulling rate on the redox state and magnetic domains of Fe-Si-O glass ceramic processed by LFZ method, *Materials Research Bulletin* (2020), doi: https://doi.org/10.1016/j.materresbull.2020.110972

Impact of the pulling rate on the redox state and magnetic domains of Fe-Si-O glass ceramic processed by LFZ method

S.A. Salehizadeh[1,2*], N.M. Ferreira[2], M.S. Ivanov[3], V. A. Khomchenko[3], J. A. Paixão[3], F.M. Costa[2], M.A. Valente[2], M.P.F. Graça[2]

[1]SEG-CEMMPRE, Mechanical Engineering Department, University of Coimbra, 3030-788 Coimbra, Portugal

[2]i3N - Department of Physics, University of Aveiro, 3810-193, Aveiro, Portugal

[3]CFisUC, Department of Physics, University of Coimbra, 3004-516 Coimbra, Portugal

***Corresponding author: ali.salehizadeh@dem.uc.pt**

Graphical abstract

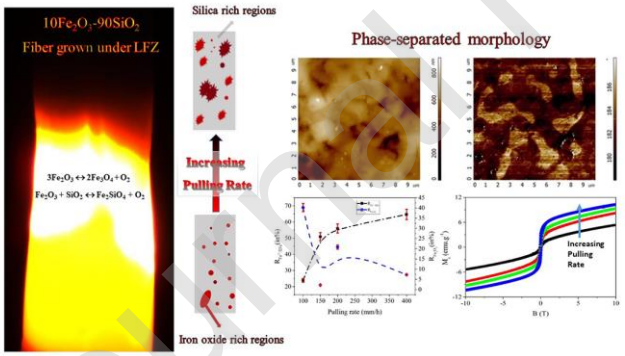

Highlights

- The Fe-Si-O glass ceramics were prepared by Laser Floating Zone (LFZ) technique.
- The influence of pulling rate variation on the crystallization kinetics and the redox state is investigated.

- Faster growth favors the formation of Fe-containing clusters with higher Fe^{2+}/Fe_{total} ratio.
- The ZFC-FC curves of the fibers showed a superparamagnetic-like behavior, characterized by a maximum, $T_{P,}$ near to the Verwey transition.
- Fitting of a modified Kneller equation on the experimental data confirms the formation of non-uniaxial interacting Fe_3O_4 clusters in the fibers grown at higher pulling rates.

Abstract

This work studies the effect of the pulling rate, varying from 100 to 400 mm/h, on the redox state, structure and magnetic properties of iron oxide bearing silica glasses processed by **laser floating zone** (LFZ) method.

XRD analysis revealed that the maximum crystallinity is obtained in the **fibre** grown at the lowest pulling rate. A detailed Raman analysis demonstrated that the global content of Fe^{2+} increases with pulling rate, while the growth under a lower pulling rate promotes the α-Fe_2O_3 crystallization. Atomic/magnetic force microscopy provided further evidence of phase-separated iron oxide crystallites formation with a high Fe^{2+}/F_{total} ratio as the pulling rate increases.

The magnetic measurements performed over a wide temperature range showed that the highest magnetization is found in the **fibre** grown at the highest pulling rate. A strong correlation between structural-topographical features and the magnetic characteristics of the glass **fibre**s is substantiated.

Keywords: Laser floating zone (LFZ); Iron oxide doped silica glass; Redox state; Atomic/Magnetic Force Microscopy (AFM/MFM); Magnetic properties.

1. Introduction

Incorporation of iron oxide particles into silica-based glasses have gained increasing **interest** due to their unique physical and chemical properties, including chemical durability, abrasion resistance, specific electromagnetic absorption features and biocompatibility [1-5]. **These advantageous characteristics have brought great merit for iron oxide containing silica glass- glass-ceramics to be employed in a wide variety of emerging industrial and technological applications; for**

instance, magnetic hyperthermia and targeted drug delivery [2, 3], microwave and electronic devices, catalysts and also sensors [1, 5]. Regardless of the original oxidation state of the iron in the starting glass batch, the final glass contains Fe^{3+} ions, with tetrahedral and octahedral coordination, and Fe^{2+} ions in octahedral coordination [6-8]. Iron (III) oxide, ferric oxide, can be found in four polymorphs; α-, β-, γ- and ε-Fe_2O_3 [9]. Being isostructural with corundum, hematite is the most stable iron (III) oxide substance and has a canted antiferromagnetic nature at room temperature. Hematite undergoes to Morin transition, T_M, and the Neel transition, T_N, at 260 K and 956 K, respectively [10, 11]. Maghemite, γ-Fe_2O_3, is a cubic spinel and ferrimagnetic at 300 K with an estimated Curie temperature, T_C, of 985 K [11]. γ-Fe_2O_3 is easily transformed to hematite at temperatures above 800 K [11-13]. Two other iron (III) oxides are thermodynamically unstable and their stable monophasic crystallites can only be formed in nanometric scale and under specific synthetic circunstances [9, 10, 14].

On the other side, magnetite, Fe_3O_4, contains both Fe^{2+} and Fe^{3+} valence states acquiring the highest magnetization among other iron oxides (82-100 $emu.g^{-1}$ when it is in the bulk form.) [1, 11, 13]. Magnetite has an inverse spinel structure in which all tetrahedral sites are occupied by Fe^{3+} ions ("A" sites), and the octahedral sites by both Fe^{3+} and Fe^{2+} states ("B" sites). The two characteristic temperatures of magnetite are T_C= 850 K and the Verwey temperature, T_V, at 120 K where a metal-insulator transition occurs [11, 13]. Ferrous oxide (iron (II) oxide), known as wustite possess a cubic structure and exhibits antiferromagnetic behaviour below the Néel temperature of 200 K [13]. From **the** thermodynamic point of view, this phase is disproportionated to α-Fe and Fe_3O_4 when cooled slowly to temperatures lower than 567 ^oC [15]. However, there are several reports regarding the formation of the metastable wustite via the reduction of hematite [16] and or silica-supported iron catalyst annealed at air [17].

Up to now, various techniques including chemical methods such as sol-gel, co-precipitation [1, 3] and/or high-temperature processing methods like laser ablation, melt-quenching and laser processing [5, 7] have been used to produce iron oxide doped glass-ceramics. Among them, laser floating zone (LFZ) method was found as a powerful processing technique enabling to prepare **not only the glass-ceramic materials [7] but also** high-quality single crystals [18-20], eutectic

structures [3, 21-23] and highly oriented polycrystalline materials [23-26]. Moreover, by providing conditions for a self-supported molten zone, the LFZ method has merit over other high-temperature synthesis approaches to avoid contamination and impurities resulted from high-temperature interaction with crucibles or other materials [27]. On the other hand, LFZ method allows us to deeply study phase transformation kinetics [7, 28-31], tuning the states of the redox-active cations diffusion phenomena [30-32] and crystallization/vitrification mechanisms in the glass **fibres** [27, 28]. Previous investigations have addressed the significant impact the chemical composition, the ambient atmosphere, composition, pulling rate on the shape, phase composition, morphology and the related characteristics of the samples grown by LFZ method [27-32]. Furthermore, it is suggested that the crystallization during the LFZ processing, strongly depends on the thermal gradient near the melt/solidification interface and the pulling rate [26]. However, understanding of the clustering and nucleation process accompanied by relevant microscopic and macroscopic changes imposed by temperature gradients during the LFZ procedure still is very inconclusive and challenging. **Previously studies had revealed** that the incorporation of up to 8% (in mol%) iron oxide into the magnesium aluminosilicate (MAS) glass **fibre**s prepared by LFZ method only presents paramagnetic attribute at room temperature likely due to poor clustering of the nano-sized iron oxide species and huge directional crystallization of non-magnetic components [27]. **Moreover,** it was demonstrated that even **through** Mossbauer spectroscopy, the estimation of the Fe^{3+}/Fe^{2+} ratio in the above-mentioned glasses is hardly attainable because of the strong overlap of the sextets due to Fe^{2+} and Fe^{3+} in the iron oxides clusters [7]. **From these studies [7, 27] it was found that only above 8% mol of Fe, magnetic phases of iron clusters, are formed in the glass matrix.**

Therefore, in the present work, $10Fe_2O_3$-$90SiO_2$ glass **fibres were grown using the** LFZ method**. The aim of this paper to study how the redox state changes as the pulling rate vary** from 100 to 400 $mm.h^{-1}$**. The influence of Fe^{2+}/Fe^{3+} redox interactions on structural, topological and magnetic characteristics of the glass fibres will also be investigated. To do so, the** as-grown **glass fibres will be** analyzed using X-ray diffraction (XRD), Raman spectroscopy, atomic force microscopy/magnetic force microscopy (AFM/MFM) and vibrating sample magnetometer (VSM) measurements.

2. Experimental

The starting powders of SiO_2 and Fe_2O_3 (MERK, purity >99.99 %) were initially mixed in an agate ball mill, during 40 min at 250 rpm, in the proportion of 90 and 10 (mol %), respectively. After that, an organic binder (PVA – Polyvinyl alcohol) was added to the mixture and the precursor rods were obtained from cold extrusion to be used as feed and seed precursors for the sample growth by the LFZ method.

The sample processing was carried out in the LFZ setup [7], equipped with a continuous CO_2- Spectron SLC laser (λ=10.6μm; 200W) in the air atmosphere. Keeping the rod diameter constant at 1.75 mm, the samples were grown at the rates of 100, 150, 200 and 400 mm/h to yield dense glass-ceramics. Thus, the glass-ceramic **fibres** are labelled as LFZ100, LFZ150, LFZ200, and LFZ400 in which the number means the pulling rate of each sample.

X-ray diffraction (XRD) was performed using an X'Pert MPD Philips diffractometer (Cu Kα radiation, λ = 0.154056 nm, 2θ=5–70°, step 0.04° and exposition 1.3 s) at 40 kV and 30 mA. The obtained diffractograms were analyzed using the JCPDS database. The Raman spectroscopy of the **fibres** was carried out in an HR800 Jobin Yvon SPEX spectrometer, using an Ar laser (λ = 532 nm) as excitation font. The spectra were obtained between 200 and 1100 cm^{-1} at room temperature in backscattering geometry.

Surface morphology and local magnetic properties were studied using an INTEGRA Aura (NT-MDT SI) scanning probe microscope equipped by the magnetic probe MFM01 (70 kHz, 3 N/m).

The magnetic properties were measured with a VSM from Cryogenics with the axis of the sample parallel to the direction of the applied magnetic field as a function of temperature, $25 \leq T \leq 300$ K, with an applied magnetic field of 0.1 Tesla in the field cooling (FC) and zero field cooling (ZFC) modes. The magnetization versus magnetic field ($-10 T \leq H \leq 10$ T) was measured at several temperatures between 25 and 300 K.

3. Results and discussion

Figure 1 exhibits the X-ray diffraction (XRD) patterns of LFZ powdered **fibre**s. According to the reflection peak positions and relative intensities, the XRD patterns show the presence of M: magnetite - Fe_3O_4 (ICDD: 00-019-0629), IS: iron silicate - Fe_2SiO_4 (ICDD: 01-070-1861), F: fayalite – 2(FeO). SiO_2 (ICDD: 00-011-0262), H: hematite - α-Fe_2O_3 (ICDD: 00-001-1053), γ: maghemite - γ-Fe_2O_3 (ICDD: 01-070-1861), W: wustite - F_xO, with $0.83 \leq x \leq 0.95$, (ICDD: 01-074-1880) phases in all samples.

It should be noted that no crystalline phase of silica was detected in the XRD patterns of the **fibre**s. The appearance of a broad hump around $2\Theta = 21^o$, characteristic of the silica glasses with the short-range order [33], is confirmed in the samples LFZ100 and LFZ150. Whereas, the formation of silica vitreous structure is not observed in LFZ200 and LFZ400. In the following, we present the reduction-oxidation reactions occurring during the LFZ process to understand the findings obtained from XRD analysis.

As described in the experimental procedure, the raw materials are SiO_2 and Fe_2O_3 powders. In a reducing atmosphere, such as the high temperature melting zone during the LFZ preparation [29], the conditions met for the formation of fayalite - Fe_2SiO_4 or iron silicate (Eq. 1 and 2), Wustite - F_xO (Eq. 3) and Magnetite - Fe_3O_4 (Eq. 4) follow as:

$$2Fe_2O_3 + 2SiO_2 \leftrightarrow 2Fe_2SiO_4 + O_2 \quad (1)$$

$$3Fe_2SiO_4 + O_2 \leftrightarrow 2Fe_3O_4 + 3SiO_2 \quad (2)$$

$$2Fe_2O_3 \leftrightarrow 4FeO + O_2 \quad (3)$$

$$3Fe_2O_3 \leftrightarrow 2Fe_3O_4 + O_2 \quad (4)$$

According to Eq. 1 and 2, the decreasing in the pulling rate and the longer time for oxidation can attribute in the formation of a lower quantity of fayalite or iron silicate, with more silica melt for the formation of glass, originating for the wide hunch at LFZ100 and LFZ150 XRD patterns. Therefore, the melting made in air at atmospheric pressure, i.e., an oxidative atmosphere, may cause the decomposition of

fayalite with the crystallization of hematite (Eq. 1) and magnetite (Eq. 2). Moreover, the hematite can be reduced into wustite and magnetite (Eq. 3 and 4 respectively).

As seen in Figure 1, the major part of the peaks detected can be attributed to more than one crystalline phase. This fact only allows us to calculate the size of the crystallites of the Wustite, F_xO, which has the diffraction peak with the greatest intensity at $2\Theta = 43.6^o$, using Scherrer's equation

$$D = K\,\lambda/(\beta\, cos\Theta) \qquad (5)$$

where λ is X-ray wavelength, K a constant, β is line broadening measured at the half-height from the most intense peaks of XRD and θ is Bragg angle. The results of this calculation (Figure 2) show that the Wustite crystallites have nanometer dimensions and their size diminish with the decreasing of the pulling rate with the minimum size for the sample LFZ150 and a little greater for the LFZ100 sample.

The main peak of the fayalite phase ($2(FeO).SiO_2$) at $2\Theta \cong 31.59^o$ is observed in all the samples. The peak at $2\Theta \cong 33.27^o$ corresponds to hematite (α-Fe_2O_3) and increases with the decrease in the growth rate of the **fibres**. The peak at $2\Theta \cong 57^o$ can be ascribed to the maghemite (γ-Fe_2O_3) phase and diminishes with the decrease of the pulling rate.

It is noteworthy that the observed broadening in XRD lines with the increasing of the pulling velocity can be interpreted in terms of lower crystallinity of these samples. However, the major problem is that the observed peaks with higher intensity may have contributions of several crystalline phases. Thus, the peak at $2\Theta \cong 35.5^o$ can be the overlapping of peaks due to magnetite, hematite, wustite and iron silicate crystalline phases and the diffraction peak at $2\Theta \cong 62.6^o$ can be attributed to magnetite, hematite, wustite phases in the sample.

Based on the XRD results, **we have shown the heterogeneous crystallization of magnetic phases containing both Fe^{2+} and Fe^{3+} oxidation states. However,** it is hard to **justify** how the **Fe^{2+}/Fe^{3+} redox ratio changes** as a function of the growth rate. **Therefore, more precise charcterization is needed to identify the environment of iron ions distributed in the glass matrix.** For this purpose, Raman spectroscopy, commonly used for determination of the structure, environment, and dynamics of glassy materials, was performed.

The experimental Raman spectra of all **fibre**s obtained at room temperature are demonstrated in Figure 3. For each spectrum, first, the baseline was **corrected to** remove the background effect and secondly the baseline-corrected spectrum was normalized **concerning** the most intense peak in each spectrum. The Raman spectra were deconvoluted into individual Gaussian **peaks to** identify and assign all possible vibration bands, as described precisely in [34]. All observed vibration bands were identified by comparison with the literature [35-47] data and **labelled** in alphabetic order and their corresponding assignments are given in Table 1.

According to the Raman analysis, all **fibre**s, **except for** LFZ150 **fibre**, showed a band around 220 cm^{-1} (Figure 3 - labeled by A) that can be ascribed to the A_{1g} mode in α-Fe_2O_3 crystallite [26]. In LFZ 150 **fibre** there is no evidence of band at ~ 620 cm^{-1} (Figure 3) assigned to E_g mode for hematite phase. These two peaks are attributed to hematite and do not have any contribution from maghemite or magnetite phases [36]. The absence of these two peaks can be related to structural changes within LFZ150 accompanied by hindering of formation of α-Fe_2O_3 phase [37]. Oppositely, the band F, in the range of 660-675 cm^{-1}, is a characteristic signature of magnetite [43].

Considering the band F, specific for Fe_3O_4, as a criterion for the abundance of Fe^{2+} ions in the **fibre**s, it is possible to calculate the ratio between the area of the band F and the area of the other bands due to Fe ions. The ratio $[Fe^{2+}]/[Fe_{tot}]$ for each sample was calculated from the relation:

$$R_{[Fe2+]/[Fetot]} = \text{Area [Band F]} / \sum \text{Area [Fe Bands]} \qquad (6)$$

where ∑Area[Fe Bands] is the sum of all band areas attributed to Fe structural units.

Complement this data; it is possible to calculate the relative areas of the bands **of** hematite entity, i.e., determine the **band's** A and E variation as a function of the pulling rate. We could approximately assess the fraction of hematite in **fibre**s R_{Fe2O3} from the summation of **the area of the peak of** bands A and E, designated for α-Fe_2O_3, and the total area of the bands associated with all iron species, ∑Area [Fe Bands], viz,

$$R_{Fe2O3} = (\text{Area}_{[\text{Band A}]} + \text{Area}_{[\text{Band E}]}) / \sum \text{Area}_{[\text{Fe Bands}]} \qquad (7)$$

The graph of both $[Fe^{2+}]/[Fe_{tot}]$ and $[Fe_2O_3]/[Fe_{tot}]$ ratio vs. the pulling rate is given in figure 4. The fraction hematite drops abruptly as the pulling rate increases from 100 to 150 mm/h; after a drastic increase in the proportion of hematite phase with the increase in the pulling rate up to 200 mm/h, again the fraction decreases gradually when the pulling rate.

It is also observed that the content of Fe^{2+} increases as the pulling rate of the **fibre**s increases. According to A. Moguš-Milanković et al. the consequence of the increase in $[Fe^{2+}]/[Fe_{tot}]$ ratio is the appearance of new oxygen bridging atoms [48].

It should be **considered** that it is difficult to ensure that this dependence exactly is correlated to the Fe^{3+} quantity in the **fibre** because we did not consider the bands which are assigned to all phases consisting Fe^{3+} ions [43-47]. From this graph, it is possible to infer an increase of magnetite amount with the pulling rate while the hematite decreases, which **corroborate** the result observed for hematite grown by the LFZ method [43].

From Raman analysis, it is possible to study the effect of the pulling rate on the variation of the silica structural units in LFZx (x=100, 150, 200 and 400) **fibres**. As seen in Table 1, the bands recognized in the range of 410-500 cm^{-1} and ~800-1000 cm^{-1} are attributed to Si-O-Si vibrations in silicate structural units [38-41]. Although, band J at ~960 cm^{-1} barely was detected at LFZ100. Besides that any trace of the band I was not observed for LFZ400. In fact, the bands around 850 (H), 900 (I), 950 (J) and 1100 (K) cm^{-1} correspond symmetric Si-O stretching vibrations of SiO_4 tetrahedral with four, three, two and one non-bridging oxygen atoms, respectively [49]. Therefore, it is an indicator of a random configuration of bridging and non-bridging oxygen in LFZ samples. Similar **behaviour** is most often associated with melts that contain high field charge divided by the square of the cation-oxygen distance, modifying cations (Mg^{2+}, La^{3+}) strength [50].

The type of modifying cation impacts on the distribution of the chain lengths appearing as a shift to the higher wavenumbers when the field strength of the modifying cation increases [51]. The change in the structure seen in Raman spectra is a result of the **difference in the strength** of Fe–O and more covalent Si–O bonds present in the network.

Figure 5 presents AFM and MFM scan images of the LFZ **fibre**s. The dark/bright contrast in the MFM images is associated with the magnetic interactions between a ferromagnetic tip and the iron oxide clusters formed in the LFZ **fibres**. The AFM images confirm the phase separation, and a similar observation was done by SEM micrographs (not shown here). The obtained MFM results demonstrate an alteration of the magnetic domain structure as the pulling rate increases. Generally, the samples LFZ100 and LFZ150 demonstrate weak MFM contrast which is partly affected by the topography. However, the LFZ150 **fibre** exhibits the areas where MFM response is not influenced by the morphology, and the inherent magnetic domain structure can be also revealed (Figure 5b). The LFZ200 sample demonstrates a clear magnetic domain structure consisting of opposite state domains with the dimension of about 100 nm, as seen in Figure 5c. The LFZ400 **fibre** reveals clear, big and elongated monodomain states with the size of ~1 x 4 μm^2 (Figure 5d). Thus, the AFM/MFM results are fully consistent with the Raman study. The glass **fibre**s grown at the lower pulling rates, LFZ100 and LFZ150, with a low $Fe^{2+}/[Fe]_{total}$ ratio, demonstrate a stronger tendency to bulk crystallization of hematite phase presenting a poor MFM response. As the pulling rate increases, ferrimagnetic monodomains of magnetite with a high $Fe^{2+}/[Fe]_{total}$ ratio **is** formed, thus giving a strong MFM response. This observation is further supported by magnetic measurement.

The ZFC and FC curves measured, with an applied field of 0.1 T, are shown in Figure 6. The remarkable features of these curves are mentioned as follows:

(a) The ZFC curves of the samples exhibit a broad peak centered at a temperature defined as T_P **indicating the formation of superparamagnetic iron oxide clusters dispersed in the glass matrix [27].** The T_P values were determined and given in Table 2. The T_P shifts progressively towards lower temperatures and gets closer to T_V = 120 K, the Verwey transition temperature, with an increase in the pulling rate. As mentioned before in Raman studies, higher growth rate leads to an increase of Fe^{2+} content (Fe_3O_4) within the **fibre**s. Thus, the T_P **behaviour** against the pulling rate is very coherent with the results achieved from the Raman analysis. Moreover, the peak broadness is a consequence of the size distribution of **the iron oxide cluster, as confirmed by SEM analysis (not shown here),** and, in turn, the energy barriers, i.e., the spread in relaxation time occurring due to different sizes and random

orientation of anisotropy axis [52]. As the measuring temperature increases, the moments gradually become aligned along with the applied field, resulting in the enhancement of the magnetization. The temperature T_P attributes to the highest blocking temperature associated with the large population of crystallite in which moments get lined up with the particular applied field. Beyond T_P, thermal energy prevails the applied field ensuing into a reduction of magnetization value progressively.

(b) However, there are also small "anomalies" indisputable in the ZFC measurements; In the LFZ400, LFZ200 and LFZ150 ZFC graphs, a change of the slope of the curve is clear at around T_F=60 K. This change is not so evident for the LFZ100 sample. Supposedly, the detected anomaly at T_F=65 K is due to the Neel transition of fayalite [53]. In addition, the small band observed in the ZFC results of the sample LFZ200 in the vicinity of 200 K can be ascribed to the Wustite crystalline phase that is paramagnetic at room temperature with a Neel transition, T_N, at around 200-210 K. The T_N of Wustite depends on the concentration of the defects in this phase [13].

(c) The value of magnetization at any temperature increases with increase in pulling rate (invoking $Fe^{2+}/\sum Fe_{total}$ ratio increasing).

In figure 7 it can be seen the hysteresis loops (magnetic moment vs. B) at 300 K (figure 7a) and 25 K (figure 7b) of studied samples. Due to the lower thermal fluctuation of the magnetic moments, the magnetization at 25 K is clearly larger than that at 300 K for all samples. It is not observed a complete saturation of the magnetization even for the highest field (B =10 T). The inobservance of the saturation for the magnetic moment can be attributed to the surface spin disorder, the canting of spins in the ferrimagnetically ordered ferrite particles (magnetite and maghemite) [54], as well as to the antiferromagnetic and paramagnetic phases (hematite, wustite, and fayalite) present in the samples.

The maximum magnetic value measured with a magnetic field of 10 T at the room temperature vs. the pulling rate is plotted in figure 8. The maximum magnetic value increases from 5.33 to 10.26 emu/g, as the pulling rate increases from 100 to 400 $mm.h^{-1}$. The observed behavior can be correlated to the data provided by the Raman analysis and AFM/MFM scan images. As already mentioned in Raman analysis and supported by magnetic force microscopy, the $Fe^{2+}/\sum Fe_{total}$ ratio increases with

increasing the pulling rate. The $Fe^{2+}/\sum Fe_{total}$ ratio enhancement favors the double exchange interaction in Fe^{3+}-Fe^{2+} pairs in which they hop between the positive ions via the intermediate ligand (oxygen) leading to the ferromagnetic alignment of the spins of **neighbouring** ions and resultantly the total magnetization increases [11, 13].

As determined by Raman analysis and MFM studies, with a decrease in the pulling rate the $Fe^{2+}/\sum Fe_{total}$ ratio reduces and the α-Fe_2O_3 crystallization boosts, thus the double exchange interaction suppresses and the antiferromagnetic superexchange coupling between Fe^{3+} ions **promote**s [55]. Therefore, LFZ100 with a high fraction of α-Fe_2O_3, 40%, manifests a sharp drop in the total magnetization and poor MFM response compared with the other **fibre**s containing a lower quantity of hematite phase.

In addition, all **fibres** show non-vanishing coercivity even at room temperature. Therefore, the magnetic feature of the particles in spherical aggregates indicates divergence from the ideal superparamagnetic behavior, resulted from a relatively strong interparticle interaction in the **fibres** [54].

The temperature-dependence of saturation magnetization can be described by the modified Bloch's law associated with spin-wave excitations of the form [55]

$$M_S = M_S(0)\left(1-\left(\frac{T}{T_0}\right)^{\alpha}\right) \qquad (8)$$

Here $M_S(0)$ is the saturation magnetization at 0 K, T_0 is the temperature at which the spontaneous magnetization of the sample reaches zero. The exponent α is known as the Bloch's exponent where α=3/2 for bulk materials [55]. Bloch derived the $T^{3/2}$ law by considering the magnon excitation of long wave-length spin-waves at low temperatures. Several studies [56-58] reported the deviation of the saturation magnetization from Bloch's law in nanoparticles at low temperatures. The modified Bloch's law for nanoparticles was shown to have a similar form to the Bloch's law for bulk materials but with Bloch's exponent α which could have values larger and smaller than 3/2 [58, 59]. For these fits, all parameters are left free to deduce the actual contribution into the equation. Typical plots of saturation magnetizations with measuring temperature along with theoretical fits to the data based on modified Bloch's law for the **fibres** are given in figure 9. The fit parameters are illustrated in Table 2. The value of the Bloch factor is ranged from α =0.62 to 0.80 for different

fibres. The results have a significant deviation with the $T^{3/2}$ dependence of M_S, and the saturation magnetization of the **fibres** decreases much slower with increasing temperature than in the case of a bulk sample (α=1.5). This result is consistent with other results found for cobalt ferrites [57] and $Zn_xMg_{1-x}Fe_2O_4$ nanoparticles [58]. The obtained α values can be explained **based on** size-effect on the energy band structure in the density of states in the spin-wave spectrum [58].

The temperature dependence of the coercive fields in particulate media has been observed to follow Kneller's law [55-58]:

$$B_C(T) = B_C(0)\left(1-\left(\frac{T}{T_B}\right)^{\beta}\right) \qquad (9)$$

where $B_C(0)$ is the coercive field at absolute zero temperature, T_B is the block temperature, and β=0.5 is for uniaxial non-interacting single domain particles [55]. We have fitted our experimental data of B_C with the Kneller's law, and the fitting plots are shown in figure 10. We could see the good fitting of the data for the temperatures below 200 K; however, due to fluctuations in B_C that occurred at temperatures above 200 K, it was not possible to include the B_C values measured at the temperature range of 200-300 K in the fitting. The obtained results from the fitting are presented in Table 2 and figure 10. The derived values for β from the fitting are near to consistent with β=0.5. However, the theoretical values of T_B are considerably larger than the T_P values. Furthermore, the T_B increases as the pulling rate go up; unlike the pulling rate dependence of the T_P. It should be kept in mind that the Kneller equation is strictly valid for uniaxial non-interacting single domain particles. Thus, the occurrence of magnetic interactions would contribute to the detected behavior [55]. Also, the $[Fe^{2+}]/[Fe_{tot}]$ ratio increases with the pulling rate resulting in the formation of more Fe_3O_4 which is not a uniaxial material [58]. Therefore, the determination of T_B via Eq. (6) may give a larger error in the **fibre**s grown at higher pulling rate. These two factors should be taken into account to explain the observed behavior for T_B.

Moreover, we demonstrate the influence of pulling rate on the coercivity and remanence obtained at two different temperatures, 25 K, and 300 K, in Table 3. The coercivity was found to decrease with increasing the growth rate (provoking enhancing in the Fe^{2+}/Fe^{3+} ratio). The Stoner–Wohlfarth theory can explain such

trend. Based on this model, the coercivity (B_C) of single-domain particles can be expressed in respect of the anisotropy constant (K) and the saturation magnetization (M_S) as [59]:

$$B_C=2K/\mu_o M_S \quad (10)$$

where μ_0 is the permeability constant of the vacuum. Thus, the decrease of the coercivity with increasing the Fe^{2+} content within the **fibres** is consistent with both reduction in the anisotropy constant and the increase of the saturation magnetization. Opposite to B_C, the remanent magnetization is enhanced as the pulling rate rises ups. The enhancement of remanence and the reduction in B_C have a linear correlation for the **fibres** grown in the rate range of 100 to 400 mm/h, associated to decrease in the anisotropy of the **fibre**s [60].

The reduced remanence (squareness) values, $SQ=M_R/M_S$, calculated from the hysteresis loops at the 25 K and 300 K are enlisted in Table 3. They are found to be in the range of 0.1 to 0.3 which is significantly smaller than the theoretical value SQ = 0.5 indicating soft magnetic properties of the **fibres** [50].

4. Conclusion

Fibres of $10Fe_2O_3$-$90SiO_2$ were grown at 100 to 400 mm/h using the LFZ technique. Through XRD, Raman and AFM/MFM analysis, we investigated the trend of heterogeneous crystallization, redox behavior and the magnetic structure as a function of the pulling rate. Using Raman spectra, we concluded that the $Fe^{+2}/\sum Fe_{total}$ ratio increases with the pulling rate. According to AFM topography, gradual nucleation and development of spherical crystalline structures were observed by reducing the pulling rate. The acquired MFM images have shown a trend towards to the formation of the elongated magnetic monodomains and the incorporation of a high ratio Fe^{2+} ion in the crystalline structure of the **fibres** grown at the highest pulling rate (400 mm/h). The ZFC-FC curves of the **fibre**s showed a superparamagnetic-like behavior, characterized by a T_P near to the Verwey transition. However; the ZFC-FC curves are influenced by the magnetic interaction between the particles with different sizes within the **fibre**s. The increasing in magnetization with pulling rate can be correlated to the sharp increase of the Fe^{2+}/Fe_{total} ratio. The

temperature-dependence of saturation magnetization has been fitted by a modified Bloch's law, and the obtained parameters can be explained base on size-effect of the energy band structure in the density of states in the spin-wave spectrum. Also, the modified Kneller´s law has been used to account for the temperature dependence of the coercivity in the **fibres**. The obtained results from the fittings are in good consistency with Raman, and morphological studies. It was proved that the pulling rate has a crucial role in the redox state of iron ions and the formation of the magnetic domains dispersed into the glass network of the **fibres**.

CRediT authorship contribution statement:

S.A. Salehizadeh: Investigation, Formal analysis, Writing - original draft, Visualization, Writing - review & editing. **N.M. Ferreira**: Investigation, Writing - review & editing, Validation. **M.V Ivanov**: Investigation, Writing - review & editing. **V.A. Khomchenko**: Writing - review & editing, Resource. **J.A. Paixão**: Resource. **F.M. Costa**: Conceptualization, Writing - review & editing, Resource. **M.A. Valente:** Supervision, Writing - review & editing, Resource. **M.P.F. Graça:** Supervision, Writing - review & editing, Resource.

Declaration of interests

☒ The authors declare that they have no known competing financial interests or personal relationships that could have appeared to influence the work reported in this paper.

Acknowledgments

We acknowledge FEDER funds through the COMPETE 2020 Program and National Funds through FCT – Portuguese Foundation for Science and Technology under the project UIDB/50025/2020 & UIDP/50025/2020. **N.M.F acknowledges financial support through FCT – Fundação para a Ciência e a Tecnologia, I.P., in the scope of the framework contract foreseen in the numbers 4, 5 and 6 of the article 23, of the Decree-Law 57/2016, of August 29, changed by Law 57/2017, of July 19. S.A.S and M.S.I.** are grateful to FCT for financial support through the

project “MATIS - Materiais e Tecnologias Industriais Sustentáveis” (CENTRO-01-0145-FEDER-000014). V.A.K. is grateful to FCT for financial support through the FCT Investigator Programme (project IF/00819/2014/CP1223/CT0011). Access to TAIL-UC facility funded under QREN-Mais Centro project ICT_2009_02_012_1890 is gratefully acknowledged.

References

[1] **S.A. Salehizadeh, M.P.F. Graça, M.A. Valente, Effect of iron on the dielectric properties of silicate glasses prepared by sol-gel, Phys. Status Solidi C. 11 (2014) 1455–1458. doi: 10.1002/pssc.201400015.**

[2] A. Hoppe, N.S. Güldal, A.R. Boccaccini, A review of the biological response to ionic dissolution products from bioactive glasses and glass-ceramics., Biomaterials. 32 (2011) 2757–74. doi:10.1016/j.biomaterials.2011.01.004.

[3] O. Bretcanu, S. Spriano, E. Verné, M. Cöisson, P. Tiberto, P. Allia, The influence of crystallised Fe_3O_4 on the magnetic properties of coprecipitation-derived ferrimagnetic glass-ceramics, Acta Biomater. 1 (2005) 421–429. doi:10.1016/j.actbio.2005.04.007.

[4] M. Malki, V. Magnien, O. Pinet, P. Richet, Electrical conductivity of iron-bearing silicate glasses and melts. Implications for the mechanisms of iron redox reactions, Geochim. Cosmochim. Acta. 165 (2015) 137–147. doi:10.1016/j.gca.2015.05.035.

[5] R.J. Barczyński, N.A. Szreder, J. Karczewski, M. Gazda, Electronic conductivity in the SiO_2–PbO–Fe_2O_3 glass containing magnetic nanostructures, Solid State Ionics. 262 (2014) 801–805. doi:10.1016/J.SSI.2013.10.008.

[6] P.A. Bingham, J.M. Parker, T. Searle, J.M. Williams, K. Fyles, Redox and clustering of iron in silicate glasses, J. Non. Cryst. Solids. 253 (1999) 203–209. doi:10.1016/S0022-3093(99)00361-0.

[7] N.M. Ferreira, A.V. Kovalevsky, J.C. Waerenborgh, M. Quevedo-Reyes, A.A. Timopheev, F.M. Costa, J.R. Frade, Crystallization of iron-containing Si–Al–Mg–O glasses under laser floating zone conditions, J. Alloys Compd. 611 (2014) 57–64. doi:10.1016/J.JALLCOM.2014.05.118.

[8] V. Vercamer, G. Lelong, H. Hijiya, Y. Kondo, L. Galoisy, G. Calas, Diluted Fe^{3+} in silicate glasses: Structural effects of Fe-redox state and matrix composition. An optical absorption and X-band/Q-band EPR study, J. Non. Cryst. Solids. 428 (2015) 138–145. doi:10.1016/J.JNONCRYSOL.2015.08.010.

[9] R. Zboril, M. Mashlan, D. Petridis, Iron(III) Oxides from Thermal Processes Synthesis, Structural and Magnetic Properties, Mössbauer Spectroscopy Characterization, and Applications, Chem. Mater. 14 (2002) 969–982. doi:10.1021/cm0111074.

[10] Y. Masubuchi, Y. Sato, A. Sawada, T. Motohashi, H. Kiyono, S. Kikkawa, Crystallization and magnetic property of iron oxide nanoparticles precipitated in silica glass matrix, J. Eur. Ceram. Soc. 31 (2011) 2459–2462. doi:10.1016/J.JEURCERAMSOC.2011.02.016.

[11] J.M.D. Coey, Magnetism and Magnetic Materials, Cambridge University Press, 2010.

[12] S. Sakurai, A. Namai, K. Hashimoto, S. Ohkoshi, First Observation of Phase Transformation of All Four Fe_2O_3 Phases ($\gamma \rightarrow \varepsilon \rightarrow \beta \rightarrow \alpha$-Phase), J. Am. Chem. Soc. 131 (2009) 18299–18303. doi:10.1021/ja9046069.

[13] R.M. Cornell, U. Schwertmann, The Iron Oxides: Structure, Properties, Reactions, Occurrences and Uses, Second Edition, Wiley-VCH Verlag, 2004.

[14] T. Danno, D. Nakatsuka, Y. Kusano, H. Asaoka, M. Nakanishi, T. Fujii, Y. Ikeda, J. Takada, Crystal Structure of β-Fe_2O_3 and Topotactic Phase Transformation to α-Fe_2O_3, Cryst. Growth Des. 13 (2013) 770–774. doi:10.1021/cg301493a.

[15] Z. Chen, K-C. Chou, K. Morita**,** Mechanism of Metastable Wüstite Formation in the Reduction Process of Iron Oxide below 570 ^oC, Mater. Trans 57 **(2016)** 1660-1663. doi:10.2320/matertrans.M2016147.

[16] W. Liu, J.Y. Lim, M.A. Saucedo, A.N. Hayhurst, S.A. Scott, J.S. Dennis, Kinetics of the reduction of wüstite by hydrogen and carbon monoxide for the chemical looping production of hydrogen, Chem. Eng. Sci. 120 (2014) 149–166. doi:10.1016/J.CES.2014.08.010.

[17] T. Herranz, S. Rojas, F.J. Pérez-Alonso, M. Ojeda, P. Terreros, J.L.G. Fierro, Carbon oxide hydrogenation over silica-supported iron-based catalysts: Influence of the preparation route, Appl. Catal. A Gen. 308 (2006) 19–30. doi:10.1016/J.APCATA.2006.04.007.

[18] T. Ito, T. Ushiyama, Y. Yanagisawa, R. Kumai, Y. Tomioka, Growth of Highly Insulating Bulk Single Crystals of Multiferroic $BiFeO_3$ and Their Inherent Internal Strains in the Domain-Switching Process, **Cryst. Growth Des**. 11 (2011) 5139–5143. doi:10.1021/cg201068m.

[19] T. Suzuki, M. Hughes, Y. Ohishi, Optical properties of Ni-doped $MgGa_2O_4$ single crystals grown by floating zone method, J. Lumin. 130 (2010) 121–126. doi:10.1016/J.JLUMIN.2009.07.029.

[20] Z. Chen, L. Yang, Y. Hang, X. Wang, Growth and magneto-optical characteristics of cerium-doped terbium gallium garnet by the floating zone method, Cryst. Res. Technol. 50 (2015) 528–531. doi:10.1002/crat.201500007.

[21] J. LLorca, V.M. Orera, Directionally solidified eutectic ceramic oxides, Prog. Mater. Sci. 51 (2006) 711–809. doi:10.1016/J.PMATSCI.2005.10.002.

[22] **A. Salehizadeh, N.M. Ferreira, M.A. Valente, B.F.O. Costa, Magnetization and room temperature Mössabuer studies of 50Fe_2O_3-50SiO_2 and 90Fe_2O_3-10SiO_2 ceramic fibers processed by laser floating zone method, Hyperfine Interact. 241 (2019) 10. doi:10.1007/s10751-019-1664-x.**

[23] Q. Ren, H. Su, J. Zhang, W. Ma, Y. Cao, J. Chen, L. Liu, H. Fu, Directional solidification and growth characteristics of $Al_2O_3/Er_3Al_5O_{12}/ZrO_2$ ternary eutectic ceramic by laser floating zone melting, J. Mater. Sci. 52 (2017) 5559–5568. doi:10.1007/s10853-017-0860-9.

[24] J.C. Diez, E. Guilmeau, M.A. Madre, S. Marinel, S. Lemonnier, A. Sotelo, Improvement of $Bi_2Sr_2Co_{1.8}O_x$ thermoelectric properties by laser floating zone texturing, Solid State Ionics. 180 (2009) 827–830. doi:10.1016/J.SSI.2009.02.004.

[25] **F.M. Costa, N.M. Ferreira, S. Rasekh, A.J.S. Fernandes, M.A. Torres, M.A. Madre, J.C. Diez, A. Sotelo, Very Large Superconducting Currents Induced by Growth Tailoring, Cryst. Growth Des. 15 (2015) 2094–2101. doi:10.1021/cg5015972.**

[26] D. Sola, R. Balda, M. Al-Saleh, J.I. Peña, J. Fernández, Time-resolved fluorescence line-narrowing of Eu^{3+} in biocompatible eutectic glass-ceramics, Opt. Express. 21 (2013) 6561. doi:10.1364/OE.21.006561.

[27] **N.M. Ferreira, A.R. Sarabando, S. Atanasova-Vladimirova, R. Kukeva, R. Stoyanova, B.S. Ranguelov, F.M. Costa, Iron oxidation state effect on the Mg-Al- Si-O glassy system, Ceram. Int. 45 (2019) 21379–21384. doi:https://doi.org/10.1016/j.ceramint.2019.07.125.**

[28] D. Sola, R. Balda, J.I. Peña, J. Fernández, Site-selective laser spectroscopy of Nd^{3+} ions in $0.8CaSiO_3$-$0.2Ca_3(PO_4)_2$ biocompatible eutectic glass-ceramics, Opt. Express. 20 (2012) 10701. doi:10.1364/OE.20.010701.

[29] N.M. Ferreira, M.C. Ferro, M.A. Valente, J.R. Frade, F.M. Costa, A. V Kovalevsky, Unusual redox behaviour of the magnetite/hematite core–shell

structures processed by the laser floating zone method, Dalt. Trans. 47 (2018) 5646–5651. doi:10.1039/C7DT04775D.

[30] M. Geho, T. Sekijima, T. Fujii, Growth mechanism of incongruently melting terbium aluminum garnet ($Tb_3Al_5O_{12}$; TAG) single crystals by laser FZ method, J. Cryst. Growth. 275 (2005) e663–e667. doi:10.1016/J.JCRYSGRO.2004.11.048.

[31] M.C. Mesa, P.B. Oliete, V.M. Orera, J.Y. Pastor, A. Martín, J. LLorca, Microstructure and mechanical properties of $Al_2O_3/Er_3Al_5O_{12}$ eutectic rods grown by the laser-heated floating zone method, J. Eur. Ceram. Soc. 31 (2011) 1241–1250. doi:10.1016/J.JEURCERAMSOC.2010.05.004.

[32] L. Ortega-San-Martín, V. Gil, J.I. Peña, Á. Larrea, V.M. Orera, Redox behaviour and ageing of GDC-Co cermets: A comparison between lamellar and conventional cermets, Solid State Ionics. 226 (2012) 30–36. doi:10.1016/J.SSI.2012.08.008.

[33] G. Ortega-Zarzosa, C. Araujo-Andrade, M.E. Compeán-Jasso, J.R. Martínez, F. Ruiz, Cobalt Oxide/Silica Xerogels Powders: X-Ray Diffraction, Infrared and Visible Absorption Studies, J. Sol-Gel Sci. Technol. 24 (2002) 23–29. doi:10.1023/A:1015105414916.

[34] S.A. Salehizadeh, B.M.G. Melo, F.N.A. Freire, M.A. Valente, M.P.F. Graça, Structural and electrical properties of $TeO_2–V_2O_5–K_2O$ glassy systems, J. Non. Cryst. Solids. 443 (2016) 65–74. doi:10.1016/J.JNONCRYSOL.2016.03.012.

[35] D.L.A. de Faria, S. Venâncio Silva, M.T. de Oliveira, Raman microspectroscopy of some iron oxides and oxyhydroxides, J. Raman Spectrosc. 28 (1997) 873–878. doi:10.1002/(SICI)1097-4555(199711)28:11<873::AID-JRS177>3.0.CO;2-B.

[36] **A.M. Jubb, H.C. Allen, Vibrational Spectroscopic Characterization of Hematite, Maghemite, and Magnetite Thin Films Produced by Vapor Deposition, ACS Appl. Mater. Interfaces. 2 (2010) 2804–2812. doi:10.1021/am1004943.**

[37] O.N. Shebanova, P. Lazor, Raman spectroscopic study of magnetite ($FeFe_2O_4$): a new assignment for the vibrational spectrum, J. Solid State Chem. 174 (2003) 424–430. doi:10.1016/S0022-4596(03)00294-9.

[38] P. Yuan, H.P. He, D.Q. Wu, D.Q. Wang, L.J. Chen, Characterization of diatomaceous silica by Raman spectroscopy, Spectrochim. Acta Part A Mol. Biomol. Spectrosc. 60 (2004) 2941–2945. doi:10.1016/J.SAA.2004.02.005.

[39] K.J. Kingma, R.J. Hemley, Raman spectroscopic study of microcrystalline silica, Am. Mineral. 79 (1994) 269–273.

[40] A. Chopelas, Single crystal Raman spectra of forsterite, fayalite, and monticellite, Am. Mineral. 76 (1991) 1101–1109.

[41] E. Huang, C.H. Chen, T. Huang, E.H. Lin, J. Xu, Raman spectroscopic characteristics of Mg-Fe-Ca pyroxenes, Am. Mineral. 85 (2000) 473–479. doi:10.2138/am-2000-0408.

[42] P.M. Sørensen, M. Pind, Y.Z. Yue, R.D. Rawlings, A.R. Boccaccini, E.R. Nielsen, Effect of the redox state and concentration of iron on the crystallization behavior of iron-rich aluminosilicate glasses, J. Non. Cryst. Solids. 351 (2005) 1246–1253. doi:10.1016/J.JNONCRYSOL.2005.03.015.

[43] N.M. Ferreira, A. Kovalevsky, M.A. Valente, F.M. Costa, J. Frade, Magnetite/hematite core/shell fibres grown by laser floating zone method, Appl. Surf. Sci. 278 (2013) 203–206. doi:10.1016/J.APSUSC.2013.01.108.

[44] L. Slavov, M.V. Abrashev, T. Merodiiska, C. Gelev, R.E. Vandenberghe, I. Markova-Deneva, I. Nedkov, Raman spectroscopy investigation of magnetite nanoparticles in ferrofluids, J. Magn. Magn. Mater. 322 (2010) 1904–1911. doi:10.1016/J.JMMM.2010.01.005.

[45] I. Chamritski, G. Burns, Infrared- and Raman-Active Phonons of Magnetite, Maghemite, and Hematite: A Computer Simulation and Spectroscopic Study, J. Phys. Chem. B. 109 (2005) 4965–4968. doi:10.1021/jp048748h.

[46] L. Stagi, J. A. De Toro, A. Ardu, C. Cannas, A. Casu, S. Seong Lee, P. Carlo Ricci, Surface Effects Under Visible Irradiation and Heat Treatment on the Phase Stability of γ-Fe_2O_3 Nanoparticles and γ-Fe_2O_3 −SiO_2 Core–Shell Nanostructures, J. Phys. Chem. C. 118 (2014) 2857–2866. doi:10.1021/jp4115833.

[47] Y.-S. Li, J.S. Church, A.L. Woodhead, F. Moussa, Preparation and characterization of silica coated iron oxide magnetic nano-particles, Spectrochim. Acta Part A Mol. Biomol. Spectrosc. 76 (2010) 484–489. doi:10.1016/J.SAA.2010.04.004.

[48] A. Moguš-Milanković, A. Šantić, S.T. Reis, K. Furić, D.E. Day, Studies of lead–iron phosphate glasses by Raman, Mössbauer and impedance spectroscopy, J. Non. Cryst. Solids. 351 (2005) 3246–3258. doi:10.1016/J.JNONCRYSOL.2005.08.006.

[49] P. Colomban, A. Tournie, L. Bellot-Gurlet, Raman identification of glassy silicates used in ceramics, glass and jewellery: a tentative differentiation guide, J. Raman Spectrosc. 37 (2006) 841–852. doi:10.1002/jrs.1515.

[50] P. Richet, B. Mysen, Silicate Glasses and melts, Silicate Glasses and Melts, 1st edition, Volume 10, Elsevier Science, 2005.

[51] R.K. Brow, Review: the structure of simple phosphate glasses, J. Non. Cryst. Solids. 263–264 (2000) 1–28. doi:10.1016/S0022-3093(99)00620-1.

[52] S. Thota, J. Kumar, Sol–gel synthesis and anomalous magnetic behaviour of NiO nanoparticles, J. Phys. Chem. Solids. 68 (2007) 1951–1964. doi:10.1016/J.JPCS.2007.06.010.

[53] F. Belley, E.C. Ferré, F. Martín-Hernández, M.J. Jackson, M.D. Dyar, E.J. Catlos, The magnetic properties of natural and synthetic $(Fe_x, Mg_{1-x})_2 SiO_4$ olivines, Earth Planet. Sci. Lett. 284 (2009) 516–526. doi:10.1016/J.EPSL.2009.05.016.

[54] R. Zamiri, S.A. Salehizadeh, H.A. Ahangar, M. Shabani, A. Rebelo, J. Suresh Kumar, M.J. Soares, M.A. Valente, J.M.F. Ferreira, Optical and magnetic properties of ZnO/$ZnFe_2O_4$ nanocomposite, Mater. Chem. Phys. 192 (2017) 330–338. doi:10.1016/J.MATCHEMPHYS.2017.01.066.

[55] S. Larumbe, C. Gómez-Polo, J.I. Pérez-Landazábal, J.M. Pastor, Effect of a $(SiO)_2$ coating on the magnetic properties of Fe_3O_4 nanoparticles, J. Phys. Condens. Matter. 24 (2012) 266007. doi:10.1088/0953-8984/24/26/266007.

[56] I.M. Obaidat, B. Issa, B.A. Albiss, Y. Haik, Investigating Negative Magnetization and Blocking Temperature in Aggregates of Ferrite Nanoparticles, IOP Conf**. Ser.:** Mater. Sci. Eng. 92 (2015) 12011. doi:10.1088/1757-899x/92/1/012011.

[57] C. Vázquez-Vázquez, M.A. López-Quintela, M.C. Buján-Núñez, J. Rivas, Finite size and surface effects on the magnetic properties of cobalt ferrite nanoparticles, J. Nanoparticle Res. 13 (2011) 1663–1676. doi:10.1007/s11051-010-9920-7.

[58] P. Masina, T. Moyo, H.M.I. Abdallah, Synthesis, structural and magnetic properties of $Zn_xMg_{1-x}Fe_2O_4$ nanoferrites, J. Magn. Magn. Mater. 381 (2015) 41–49. doi:10.1016/J.JMMM.2014.12.053.

[59] C. R. Vestal, Z. John Zhang, Synthesis of $CoCrFeO_4$ Nanoparticles Using Microemulsion Methods and Size-Dependent Studies of Their Magnetic Properties, Chem. Mater. 14 (2002) 3817–3822. doi:10.1021/cm020112k.

[60] J.F. Qian, A.K. Nayak, G. Kreiner, W. Schnelle, C. Felser, Exchange bias up to room temperature in antiferromagnetic hexagonal Mn_3Ge, J. Phys. D. Appl. Phys. 47 (2014) 305001. doi:10.1088/0022-3727/47/30/305001.

Figure Captions

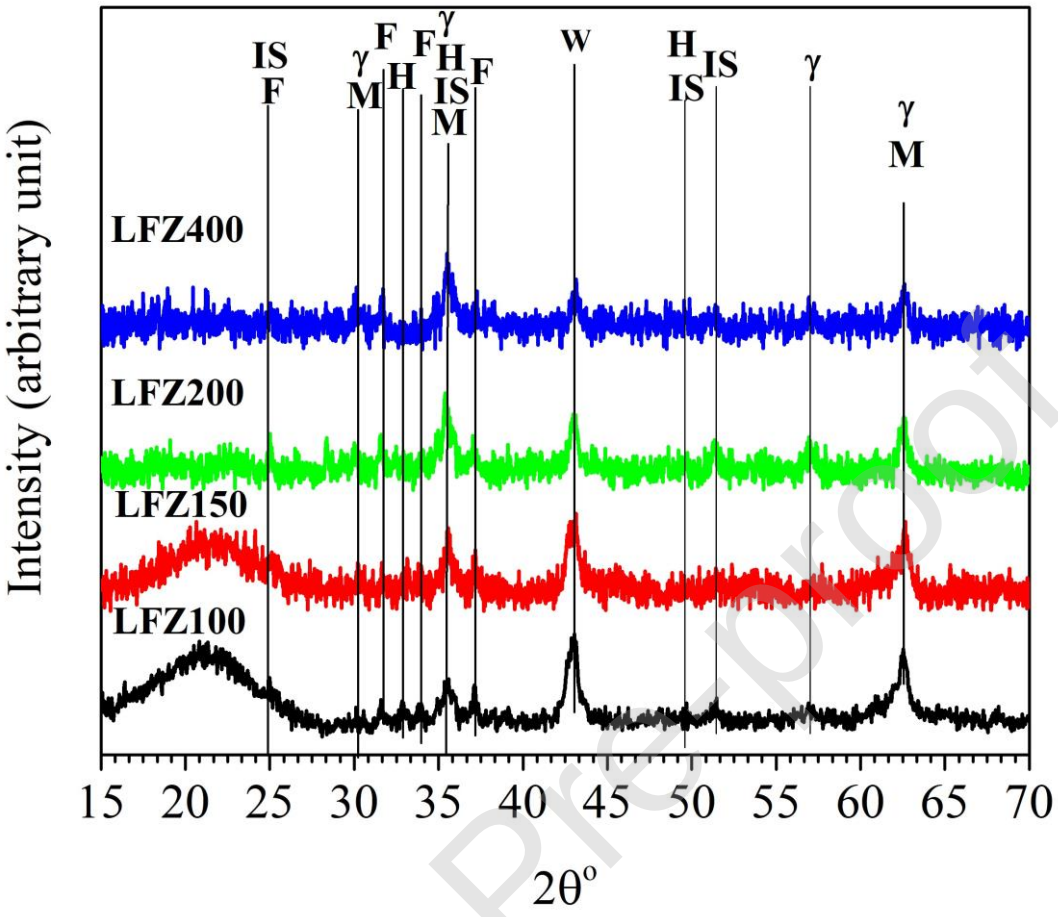

Figure 1) XRD patterns of all powdered **fibres.** M: Magnetite - Fe_3O_4 (ICDD: 00-019-0629), IS: iron silicate - Fe_2SiO_4 (ICDD: 01-070-1861), F: Fayalite - 2FeO. SiO_2 (ICDD: 00-011-0262), H: Hematite - α-Fe_2O_3 (ICDD: 00-001-1053), γ: Maghemite - γ-Fe_2O_3 (ICDD: 01-070-1861), W: Wustite - F_xO (ICDD: 01-074-1880).

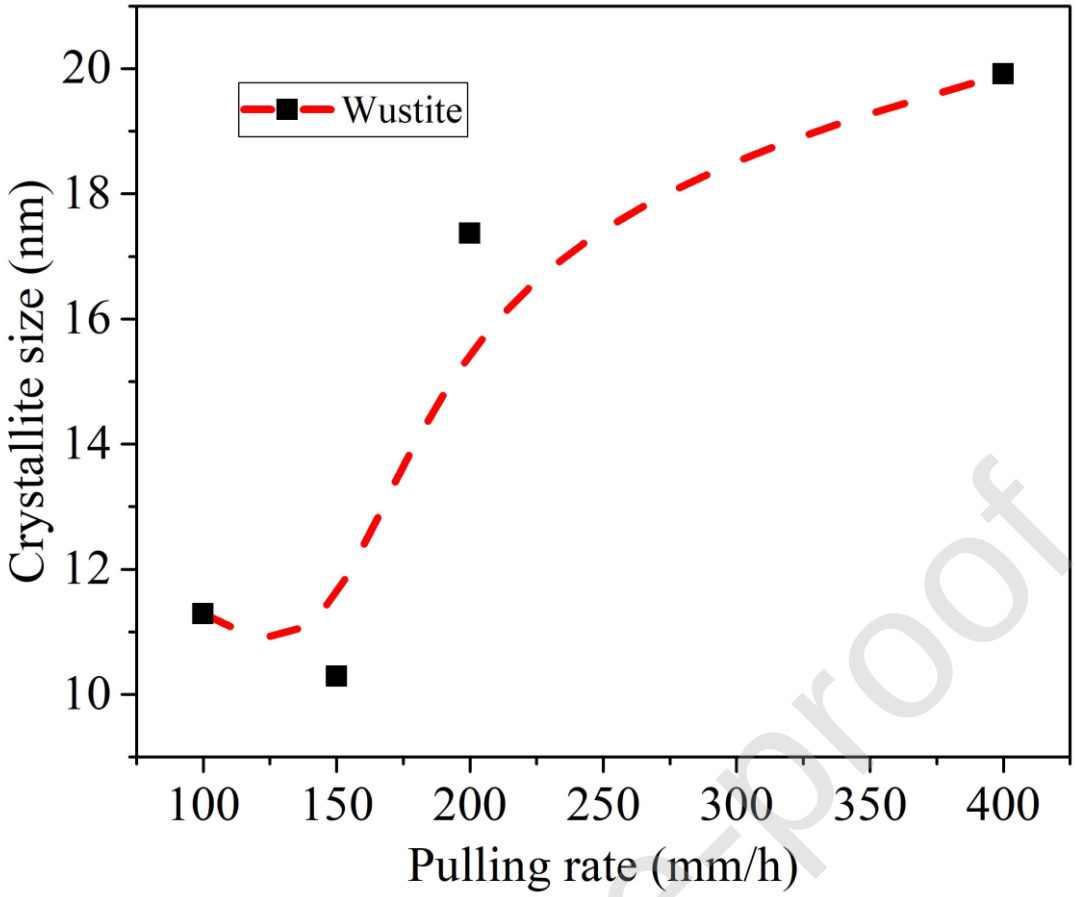

Figure 2) Crystallite size of wustite calculated using Debye-Scherer equation.

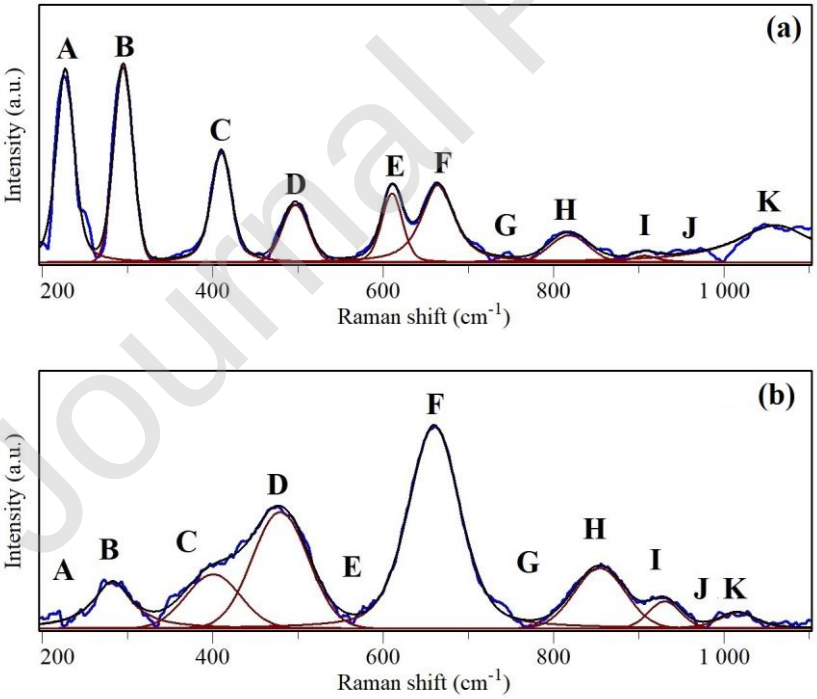

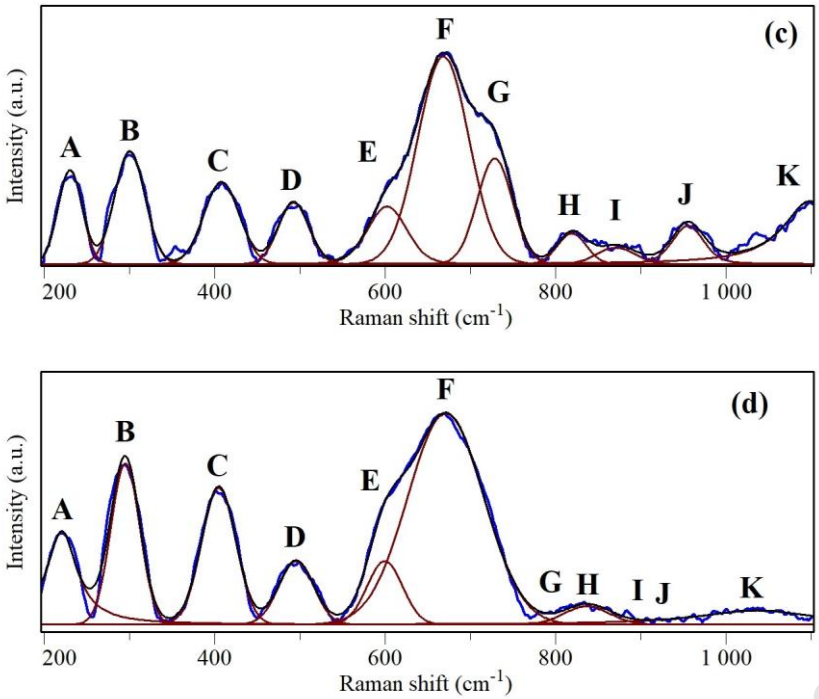

Figure 3) Normalized and deconvoluted into individual Gaussian peaks of the Raman spectra.

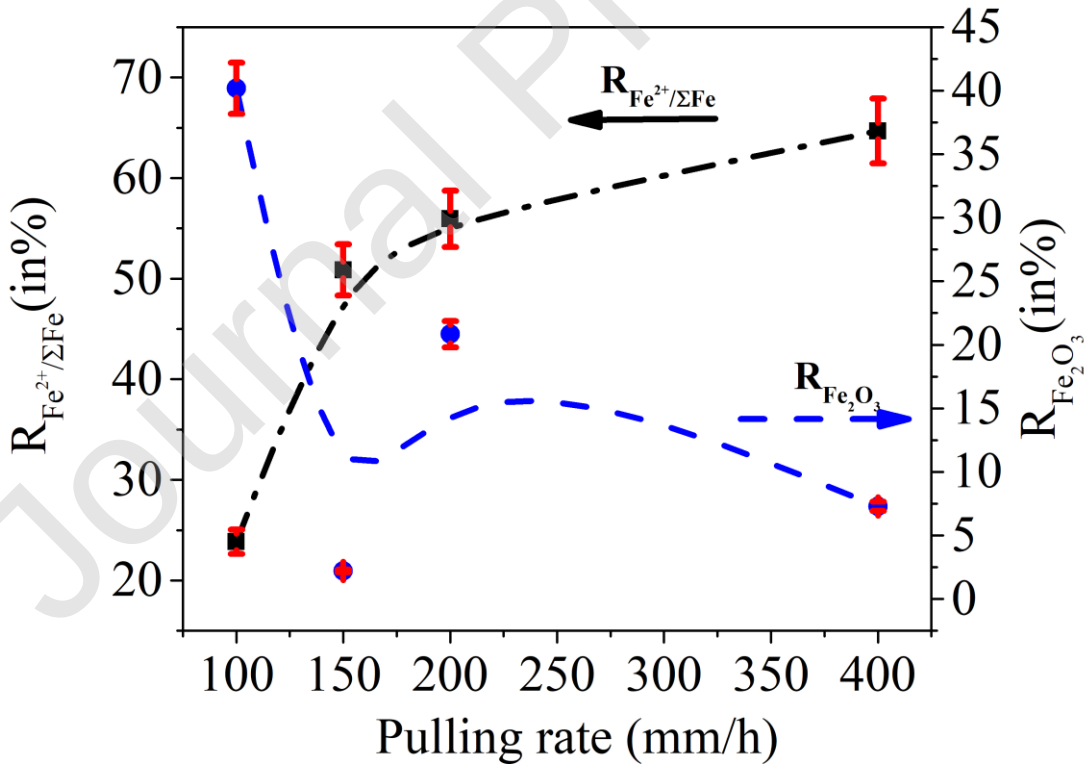

Figure 4) $[Fe^{2+}]/[Fe_{total}]$ and $R_{Fe2O3}/[Fe_{total}]$ ratio as a function of the pulling rate. (The dash lines are guides for eyes).

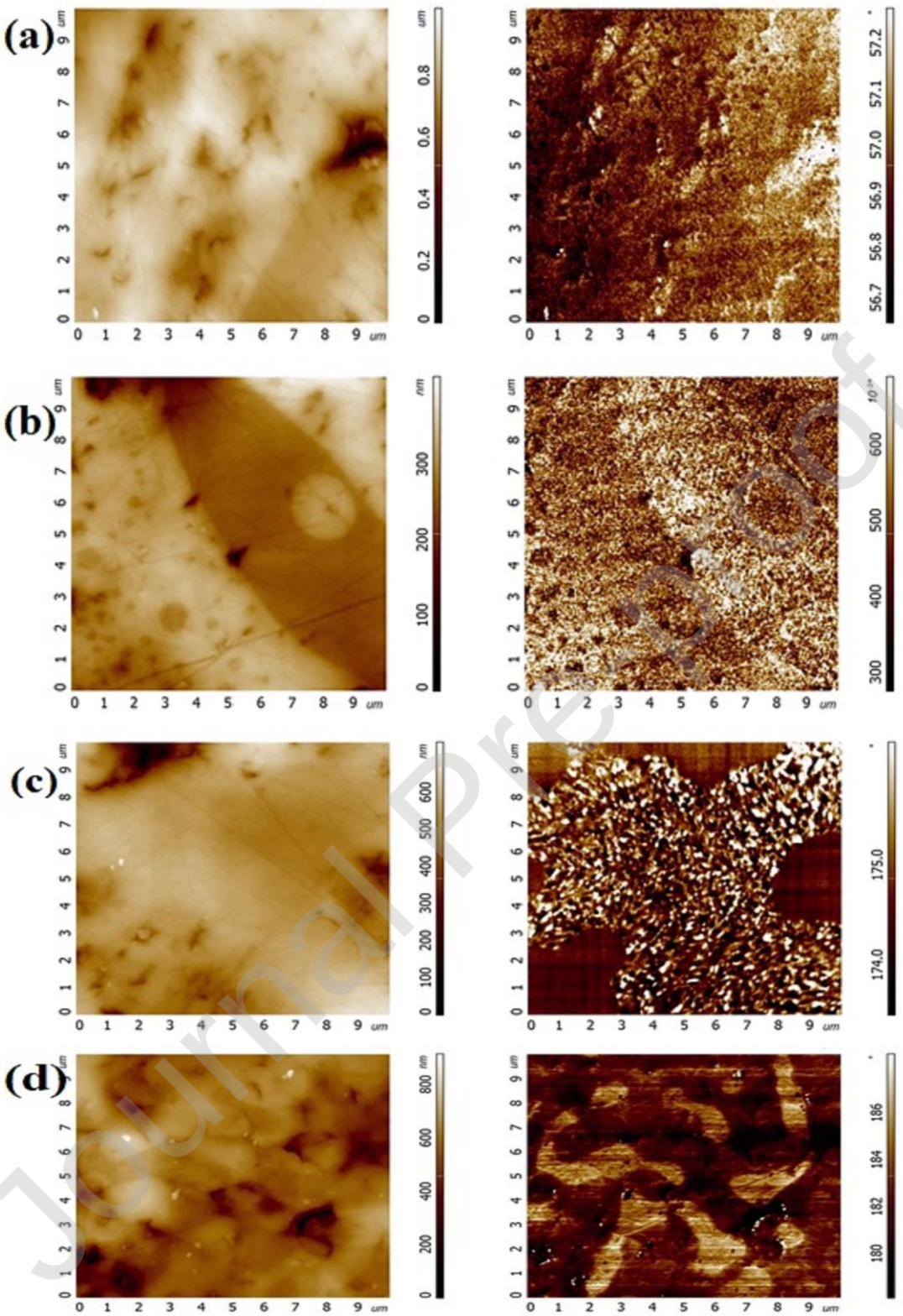

Figure 5) AFM/MFM images of a) LFZ100, b) LFZ150, c) LFZ200 and d) LFZ400 mm/h. (The topography and MFM response images are presented in the left and right panel, respectively).

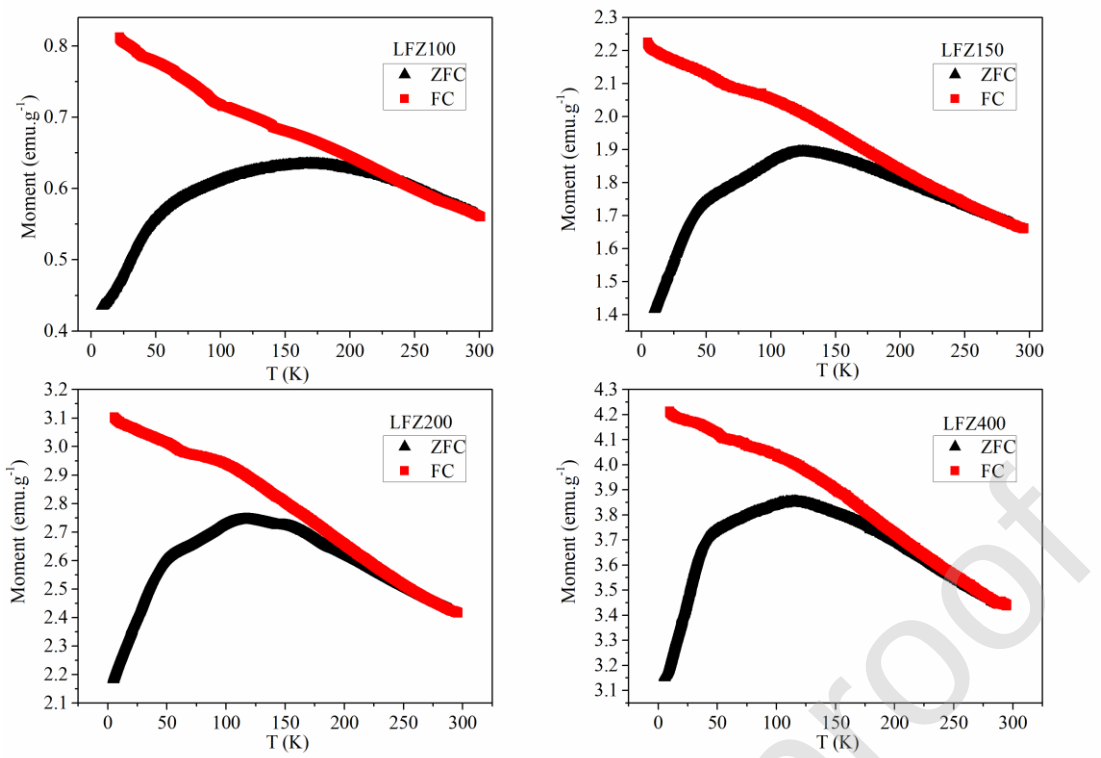

Figure 6) ZFC and FC curves measured under an applied field of 0.1 T.

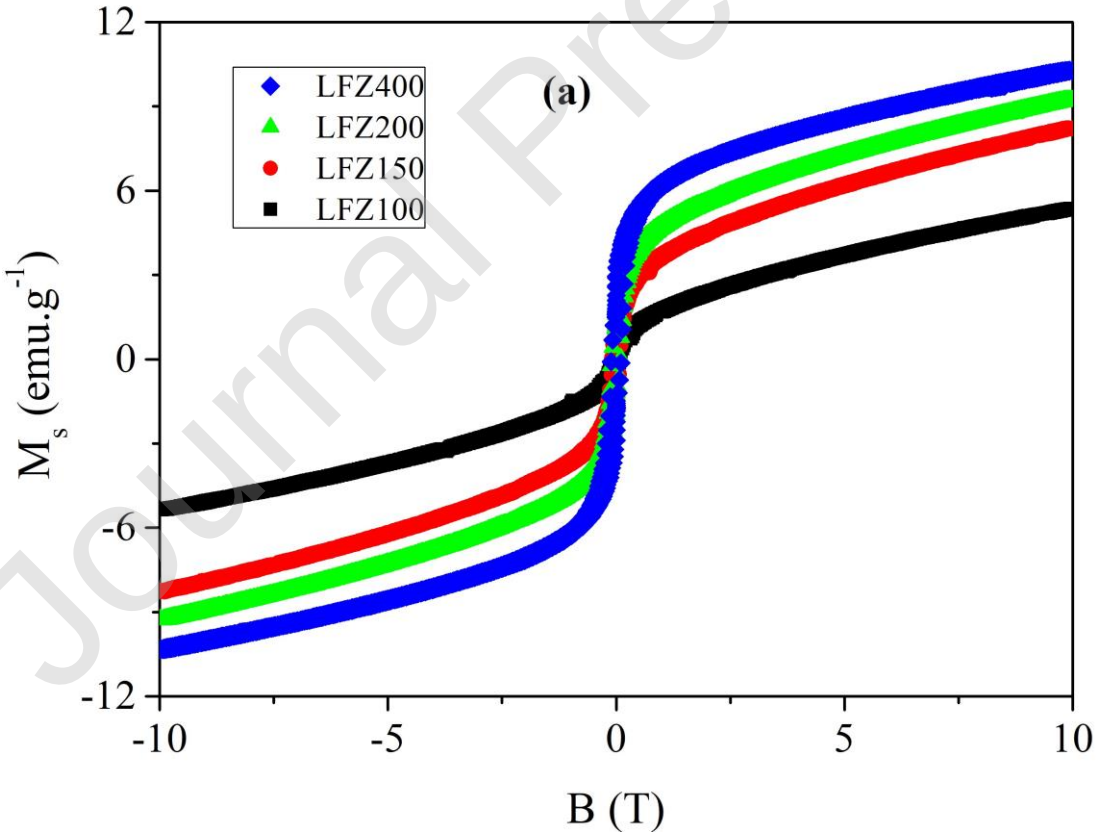

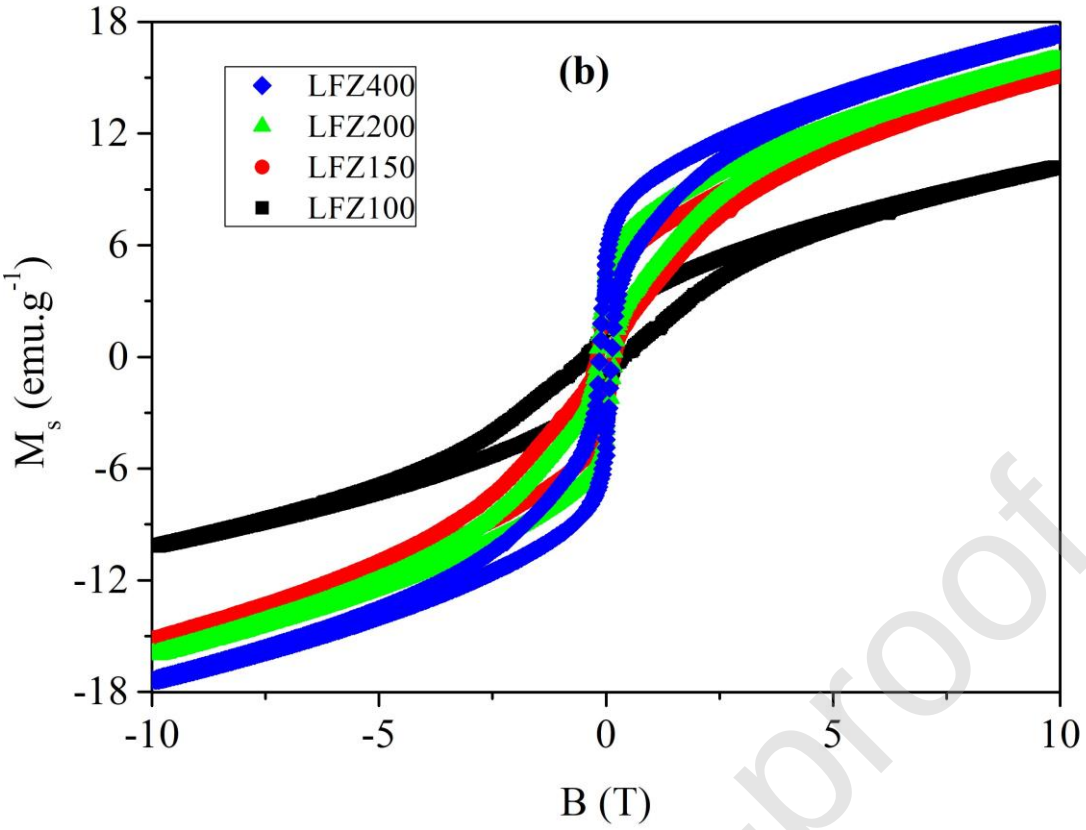

Figure 7) Magnetization curves measured at a) 300 K and b) 25 K up to maximum field 10 T for the LFZ **fibres**.

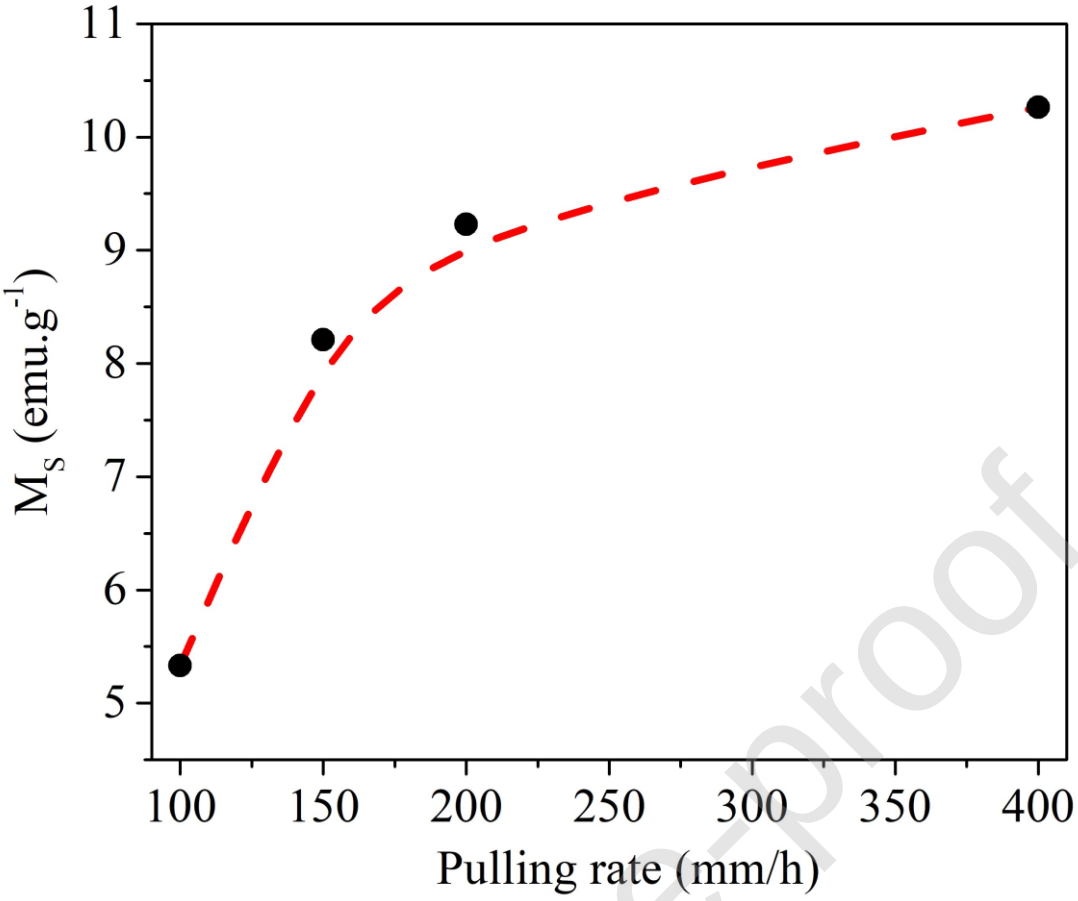

Figure 8) Dependence of the M_S value measured at room temperature on the pulling rate. (The dashed line is a guide for eyes).

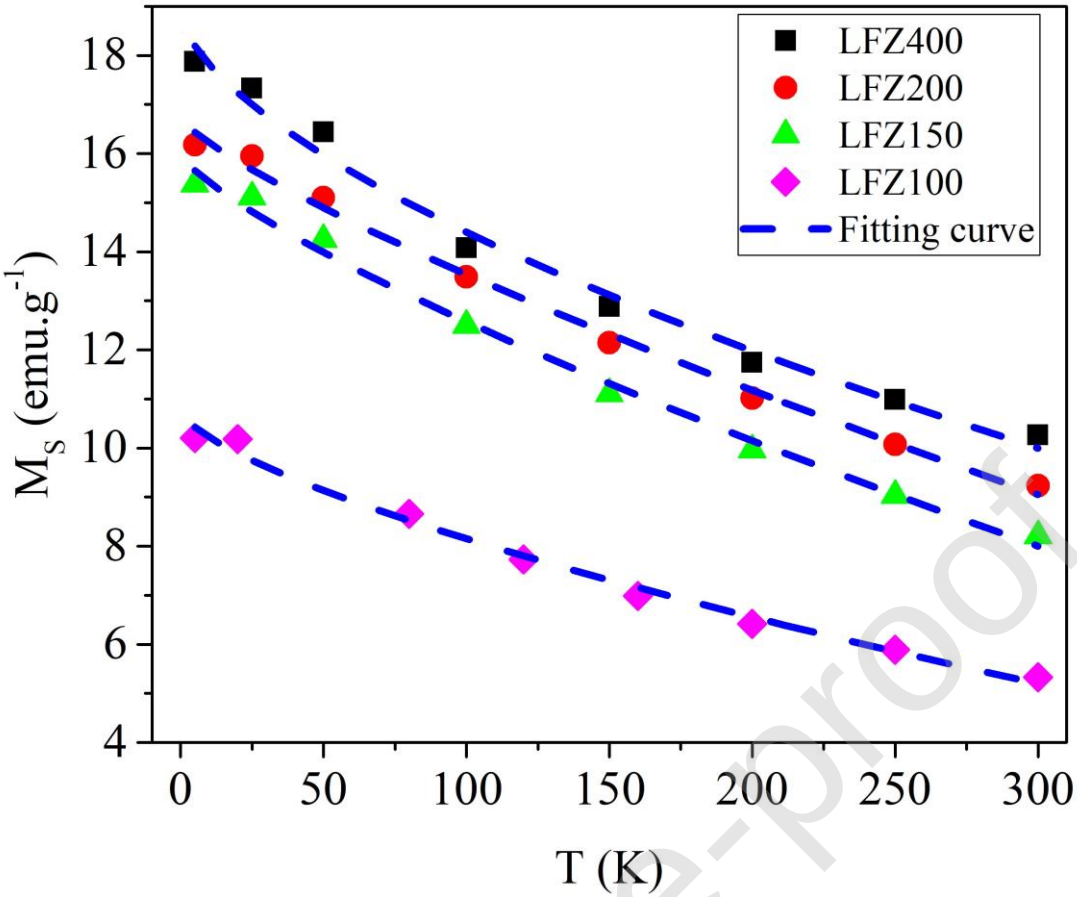

Figure 9) Saturation magnetization as a function of temperature for the LFZ **fibres.** The dashed lines showed the best-fits to experimental data based on modified Bloch's law.

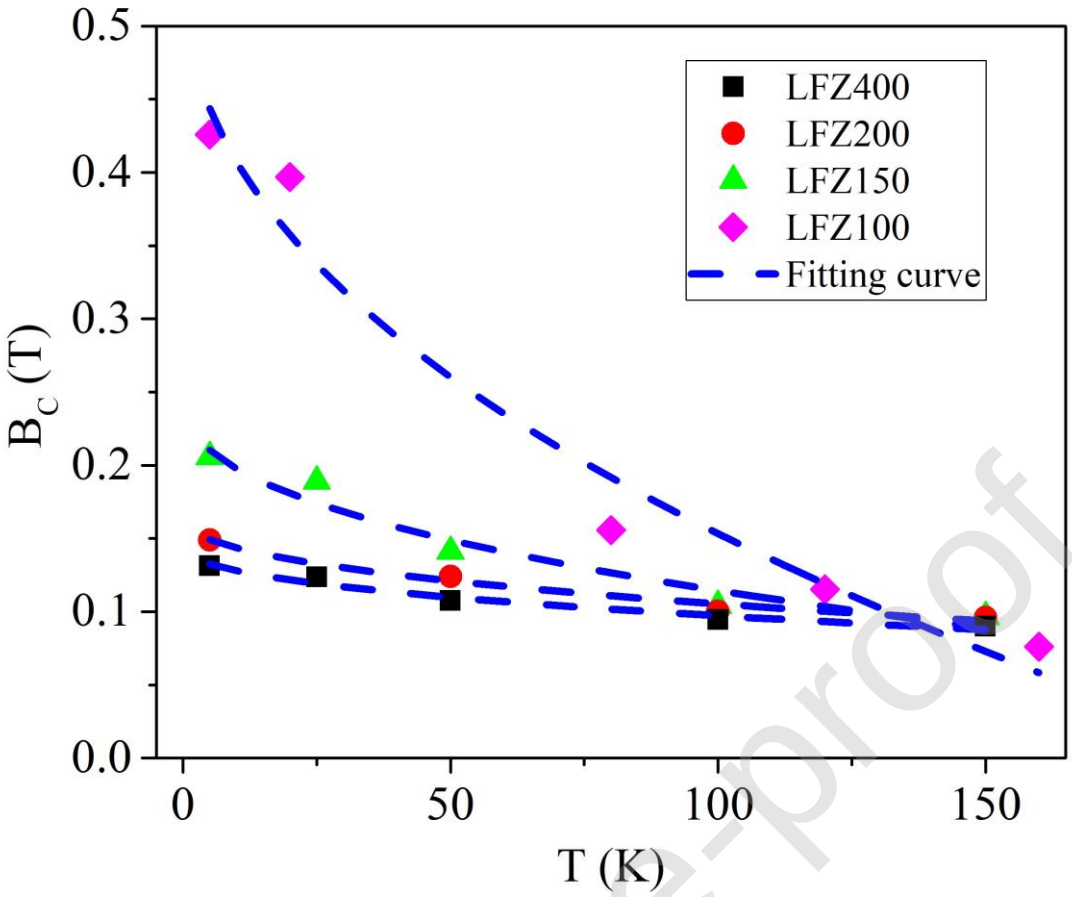

Figure 10) Fitting of the temperature dependence of coercivity based on modified Kneller's law (the dashed line).

Table Captions

Table 1) Raman bands position and corresponding assignment of the LFZ as-grown $10Fe_2O_3$:$90SiO_2$ **fibre**s [7, 15-17, 20-29].

Raman band wavenumbers (cm^{-1})					**Assignment**
Band notation	LFZ100	LFZ150	LFZ200	LFZ400	
A	225	-	231	220	Fe-O stretching bond hematite crystalline
B	295	281	300	295	asymmetric bends oxygen with respect to Fe in hematite and magnetite
C	411	394	409	401	Si-O-Si symmetric stretching bending in quartz
D	498	477	492	495	Si-O-Si bond bending vibration
E	614	-	613	601	Fe-O bond in hematite
F	663	662	673	669	A_{1g} mode in magnetite
G	-	-	731	-	$\nu_3(+\nu_1)$ vibration of SiO_4 in fayalite
H	816	858	822	830	Si-O-Fe due to distortion of silicate tetrahedra structural units
I	904	930	890	-	
J	964	-	951	-	
K	1048	1014	1037	1036	

Table 2) Parameters obtained from the fittings to the modified Bloch's law and Kneller's law, respectively, along with the experimental values of T_P.

Sample	Fitting parameters derived from the modified Bloch law				Fitting parameters derived from the modified Kneller law				T_P (K) (±1)
	$M_S(0)$ (emu.g^{-1})	α	T_0 (K)	χ^2 correlation coefficient	$B_C(0)$ (T)	T_B (K)	β	χ^2 correlation coefficient	
LFZ100	10.74	0.69	781	0.990	0.54	204	0.47	0.9837	169
LFZ150	15.99	0.77	735	0.993	0.24	418	0.44	0.9775	125
LFZ200	16.72	0.80	793	0.994	0.16	1012	0.43	0.9887	117
LFZ400	18.88	0.62	1006	0.988	0.14	1254	0.43	0.9850	114

Table 3) Experimental magnetic parameters measured at 25 K and 300 K.

Sample	@ 25 K				@ 300 K			
	Mr **(emu.g^{-1})**	Ms **(emu.g^{-1})**	Bc **(T)**	SQ	Mr **(emu.g^{-1})**	Ms **(emu.g^{-1})**	Bc **(T)**	SQ
LFZ100	1.860	10.182	0.396	0.182	0.509	5.333	0.101	0.095
LFZ150	3.533	15.093	0.189	0.234	1.643	8.199	0.101	0.200
LFZ200	4.415	15.948	0.185	0.276	2.307	9.228	0.088	0.249
LFZ400	4.907	17.330	0.123	0.283	2.894	10.263	0.105	0.282